

# A first principles TDDFT framework for spin and time-resolved ARPES in periodic systems

Umberto De Giovannini\* and Hannes Hübener†

*University of the Basque Country UPV/EHU, Nano-Bio Spectroscopy Group, Avenida de Tolosa 72, 20018 San Sebastian, Spain*

Angel Rubio‡

*University of the Basque Country UPV/EHU, Nano-Bio Spectroscopy Group, Avenida de Tolosa 72, 20018 San Sebastian, Spain and*

*Max Planck Institute for the Structure and Dynamics of Matter, Luruper Chaussee 149, 22761 Hamburg, Germany.*

*Center for Free-Electron Laser Science and Department of Physics, University of Hamburg, Luruper Chaussee 149, 22761 Hamburg, Germany*

(Dated: September 13, 2016)

We present a novel theoretical approach to simulate spin, time and angular-resolved photoelectron spectroscopy (ARPES) from first principles that is applicable to surfaces, thin films, few layer systems, and low-dimensional nanostructures. The method is based on a general formulation in the framework of time-dependent density functional theory (TDDFT) to describe the real time-evolution of electrons escaping from a surface under the effect of any external (arbitrary) laser field. By extending the so called t-SURFF method to periodic systems one can calculate the final photoelectron spectrum by collecting the flux of the ionization current through an analysing surface. The resulting approach, that we named t-SURFFP, allows to describe a wide range of irradiation conditions without any assumption on the dynamics of the ionization process allowing for pump-probe simulations on an equal footing. To illustrate the wide scope of applicability of the method we present applications to graphene, mono- and bi-layer WSe<sub>2</sub>, and hexagonal BN under different laser configurations.

## INTRODUCTION

Angular resolved photoelectron spectroscopy is one of the most prominent and mature techniques employed to probe the electronic properties of crystalline materials. In its most traditional application it allows to directly map band dispersion and Fermi surfaces of solids from the energy and momentum distribution of the escaping electrons<sup>1,2</sup>.

Following the advances in laser pulse generation and photoelectron detection techniques in the last years we have witnessed an increasing presence of ARPES experiments capable to resolve time and spin polarization degrees of freedom<sup>3,4</sup>. Time-resolved ARPES (tARPES) unlocks the time degree of freedom to study non-equilibrium dynamic of solids at the natural time scale of electronic excitations and relaxations<sup>5-9</sup>. Resolving the spin polarization of photoelectrons with spin ARPES (sARPES) provides additional information on the spin character of the sample<sup>10-13</sup>. Exploring these new dimensions offer unprecedented opportunities to test our current understanding of matter.

Currently, the most common theoretical approaches to calculate ARPES are based on the one step-model where electron photoemission is treated as a unique coherent process that include all the scattering events<sup>14</sup>. This is in contrast to the simpler three-step model where ionization is divided into three separate processes<sup>15</sup>. These approaches, largely based on many-body perturbation theory formulated in terms of Green's function, proved to be successful in many relevant cases<sup>16-19</sup>. However the perturbative approach underlying these methods is not

suitable to describe tARPES.<sup>20</sup> Including the time degree of freedom needed for tARPES requires a real time approach which, in the many-body context, is provided only by Keldysh Green's function theory. Efforts in this direction are still scarce and largely reduced to applications with model-Hamiltonians<sup>21,22</sup>, and current attempts to formulate the problem under the one-step model are still at the formal level<sup>23</sup>.

In this paper we propose a completely different and computationally efficient approach based on a real-space real-time formulation of TDDFT where we obtain the ARPES spectra by directly analyzing the photoelectron current flux through a surface using the time-dependent surface flux method (t-SURFF). The t-SURFF method is a well established technique that has been successfully employed to study ionization of atoms and small molecules under strong laser fields<sup>24-29</sup>. This method has only recently been exported to TDDFT by some of the authors<sup>30</sup>. The application of t-SURFF to surfaces ionization dynamics is completely new and in this paper we present the extension of the method to semi-periodic systems. We name the extended method t-SURFFP. The resulting approach is fully ab-initio and capable to describe situations with any number of laser fields without making any assumption on the ionization process and at a modest computational cost. For these reasons is naturally suited to simulate simulate tARPES. Furthermore, in the spirit of the one-step model, scattering and surface effects are automatically included in the formalism.

The paper is organized as follows. In Sec. I we present our method in the context of TDDFT and in the more general context of ARPES. We then proceed to validate

our technique in Sec. II where we illustrate three representative cases: graphene, WSe<sub>2</sub>, and hBN. Finally, in Sec. III we discuss our findings and present the conclusions.

Atomic units ( $\hbar = e = 1$ ) are used throughout the paper unless otherwise specified.

## I. THEORY

### A. General

We here below briefly introduce the key concepts and quantities commonly used in the field and that we will use throughout the paper.

ARPES experiments are based on electron photoemission. When a field of appropriate energy  $\omega$  irradiates a material surface a fraction of the electrons, originally bound to the crystal, is released into the vacuum as shown in Fig 1 (a). These ionized electrons emerge with a kinetic energy distribution that depends both on the external field and the material's electronic properties. Further away, at the detector, the kinetic energy distribution is measured as a function of energy  $E$  and angle  $\theta$ , to form the angular resolved photoelectron spectrum  $\mathcal{P}(E, \theta)$ . This spectrum can be equivalently expressed as a function of the escaping vector momentum  $\mathbf{p}$ ,  $\mathcal{P}(\mathbf{p})$ . In some experiments a second stage is also capable to characterize the spin polarization along an arbitrary axis  $\mathbf{s}$  and thus to measure  $\mathcal{P}_{\mathbf{s}}(\mathbf{p})$ . Finally, time resolution can be achieved employing two pulses delayed by a time  $\Delta t$  in a pump-probe setup. The time resolved spectrum,  $\mathcal{P}(\mathbf{p}, \Delta t)$ , is thus obtained by composing the spectra stroboscopically measured at different delays.

Einstein's photoelectric effect<sup>31</sup> underlies the interpretation of the physical information contained in the photoelectron spectrum represented schematically in Fig 1 (b). In fact, the kinetic energy distribution of the electrons escaping the material follows the energy conservation relation  $E = \omega - \phi - E_b$ ; where  $\phi > 0$  is the work function – the minimum energy required to promote one electron into the vacuum – and  $E_b > 0$  is the binding energy – the band energy of the electrons relative to the Fermi level. To extract one electron from the material requires a field with  $\omega > \phi$ .

From energy conservation it is thus apparent that the photoelectron spectrum contains information on the energy levels of the system. If the laser field is weak enough we can assume that momentum of the electron parallel to the surface  $\mathbf{k}_{\parallel}$  – the crystal momentum – is conserved during the ionization process. This means that at the detector  $\mathbf{p}_{\parallel} = \mathbf{k}_{\parallel}$  and thus that  $\mathcal{P}(\mathbf{p}_{\parallel}, E)$ , obtained from ARPES  $\mathcal{P}(\mathbf{p})$  with  $E = \mathbf{p}^2/2$ , directly maps to the electron dispersion in the crystal, i.e. the band structure.

This is the cornerstone of ARPES but is important to bear in mind that it is a strong idealization, useful to interpret the data, while in the reality of the experiment the picture can be more complex. Several effects present

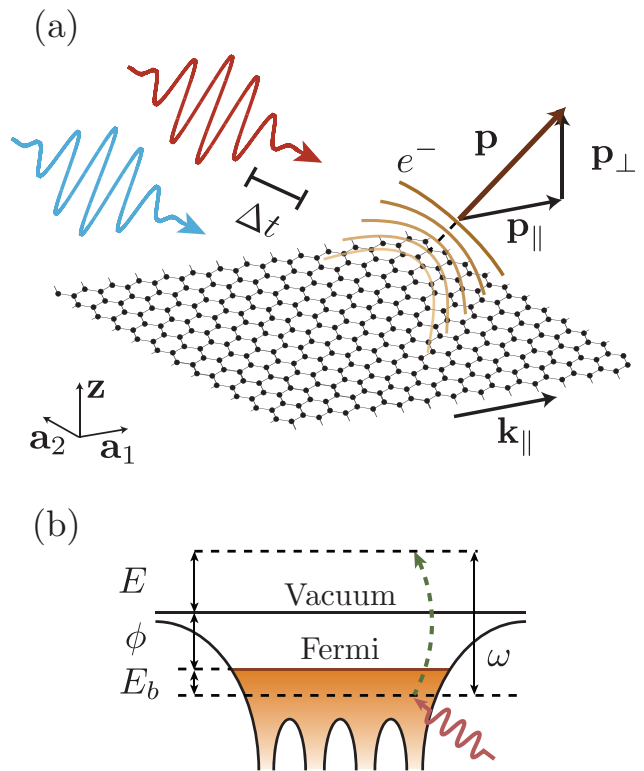


FIG. 1. Schematic cartoon for the basic ingredients of tARPES. In (a) we schematically illustrate the electron photoemission process from a surface which periodically repeats itself along the lattice vectors  $\mathbf{a}_1$  and  $\mathbf{a}_2$ . A useful picture to guide in the interpretation of ARPES is provided by the photoelectric effect depicted in (b).

in real materials may contribute to a departure from this picture. Among the most common we mention dynamical coupling to bosonic excitations such as phonons or plasmons<sup>32–34</sup> and surface effects<sup>35,36</sup>.

In this paper we take an atomistic approach to simulate the photoemission process and include in the calculation the portion of space centered around the surface, both extending in the material and in the vacuum, that is needed to describe the process. In the next section we describe the formalism, in the framework of TDDFT, to perform such a simulation and later discuss how ARPES can be obtained from the time-dependent density.

### B. Time-dependent spin-density functional theory for semi-periodic systems

In this work we describe systems with non-trivial spin configurations derived from the presence of spin-orbit coupling (SOC) and therefore we use spin-density functional theory (SDFT)<sup>37</sup>.

In SDFT the fundamental variable is the  $2 \times 2$  spin-density matrix  $\rho(\mathbf{r}) = \rho_{\alpha\beta}(\mathbf{r})$  where the greek indices span the spin space  $\alpha = +, -$ . This matrix is defined in

terms of the spinless density – or charge density –  $n(\mathbf{r})$  and the magnetization vector  $\mathbf{m}(\mathbf{r})$  as follows

$$\rho(\mathbf{r}) = \frac{1}{2}n(\mathbf{r})\sigma_0 + \frac{1}{2}\mathbf{m}(\mathbf{r}) \cdot \boldsymbol{\sigma} \quad (1)$$

with  $\boldsymbol{\sigma} = (\sigma_x, \sigma_y, \sigma_z)$  being the  $2 \times 2$  Pauli matrices and  $\sigma_0$  the identity matrix. From the definition it directly follows that the spinless density  $n(\mathbf{r})$  can be obtained by tracing the spin-density matrix over the spin dimension  $n(\mathbf{r}) = \text{Tr}(\rho(\mathbf{r}))$ .

In this work we address the modeling on electrically driven systems for which the use of TDDFT is justified, for the case of time dependent magnetic fields one should in principle use TD-current DFT<sup>38</sup>. The central principle of TDDFT is that all observables of a time-dependent many-body system can be obtained from the knowledge of its time-dependent density alone<sup>39–41</sup>. Likewise in static DFT the system of interacting particles is mapped into an auxiliary non-interacting system having the same time-dependent density, the Kohn-Sham (KS) system<sup>42</sup>. The KS system is represented by a Slater determinant composed of two-component spinors

$$\bar{\varphi}_j(\mathbf{r}) = \begin{bmatrix} \varphi_{j+}(\mathbf{r}) \\ \varphi_{j-}(\mathbf{r}) \end{bmatrix} \quad (2)$$

whose time evolution is governed by the following time-dependent KS equations (TDKS)

$$\begin{cases} i \frac{\partial}{\partial t} \bar{\varphi}_j(\mathbf{r}, t) = \hat{H}_{\text{KS}}[\boldsymbol{\rho}](\mathbf{r}) \bar{\varphi}_j(\mathbf{r}, t) \\ \hat{H}_{\text{KS}}[\boldsymbol{\rho}](\mathbf{r}) = \\ -\frac{1}{2} \left( \nabla - \frac{\mathbf{A}(t)}{c} \right)^2 \sigma_0 + V_{\text{ion}}(\mathbf{r}) + V_{\text{KS}}[\boldsymbol{\rho}](\mathbf{r}) \end{cases} \quad (3)$$

with  $\hat{H}_{\text{KS}}[\boldsymbol{\rho}](\mathbf{r})$  being the KS Hamiltonian composed of the external laser field expressed as a time-dependent vector potential in the velocity gauge  $\mathbf{A}(t)$  (with the electric field being  $\mathbf{E}(t) = \partial \mathbf{A} / \partial t$ ), the external potential generated by the ions in the lattice  $V_{\text{ion}}(\mathbf{r})$  and the KS potential  $V_{\text{KS}}[\boldsymbol{\rho}](\mathbf{r})$ . The KS potential is the sum of the classical electrostatic potential  $V_{\text{H}}[n](\mathbf{r})$ , that only depends on the spinless density, and the exchange and correlation potential  $V_{\text{xc}}[\boldsymbol{\rho}](\mathbf{r})$  responsible for the many-body interaction

$$V_{\text{KS}}[\boldsymbol{\rho}](\mathbf{r}) = V_{\text{H}}[n](\mathbf{r}) + V_{\text{xc}}[\boldsymbol{\rho}](\mathbf{r}). \quad (4)$$

Non-trivial spin configurations are induced by spin-orbit coupling (SOC) whenever heavy ions are present in the crystal. In practice this introduces a term proportional to  $\mathbf{L} \cdot \mathbf{S}$  in the ions' potential  $V_{\text{ion}}(\mathbf{r})$  that breaks spin rotational symmetry and allows for non-collinear spin configurations.

The KS Hamiltonian in (3) has a functional dependence on the spin-density matrix  $\boldsymbol{\rho}$  which can be reconstructed from the spinors using (1) and the charge density

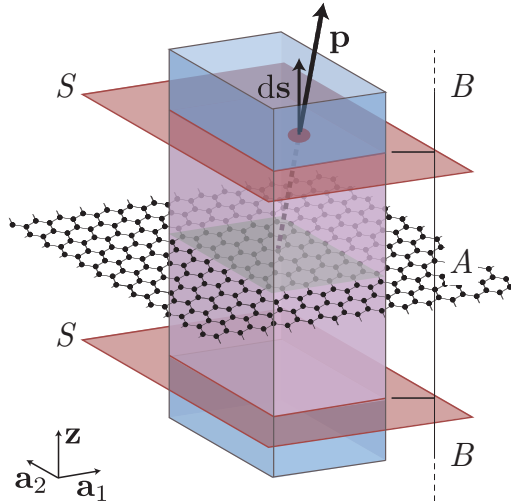


FIG. 2. Scheme illustrating the geometrical model needed to simulate the ionization process in a semi-periodic system.

and magnetization vector defined by

$$n(\mathbf{r}) = \sum_{j=1} \theta(\mu - \epsilon_j) \bar{\varphi}_j(\mathbf{r})^\dagger \bar{\varphi}_j(\mathbf{r}) \quad (5)$$

$$\mathbf{m}(\mathbf{r}) = \sum_{j=1} \theta(\mu - \epsilon_j) \bar{\varphi}_j(\mathbf{r})^\dagger \boldsymbol{\sigma} \bar{\varphi}_j(\mathbf{r}) \quad (6)$$

where  $\epsilon_j$  is the  $j$ -th eigenvalue of  $\hat{H}_{\text{KS}}[\boldsymbol{\rho}](\mathbf{r})$  and  $\mu$  is the Fermi level obtained with the constraint that the charge density integrates to the total number of electrons:  $N = \int d\mathbf{r} n(\mathbf{r})$ .

In general  $\hat{H}_{\text{KS}}[\boldsymbol{\rho}](\mathbf{r})$  is not diagonal in spin. The only diagonal term is the gauge-invariant kinetic operator – the first term of KS Hamiltonian in (3). However, in crystals composed of light atoms, for which SOC is negligible, and in absence of a magnetic field the spin-density is collinear. This means that  $\mathbf{m}(\mathbf{r})$  is constant in space and that is possible to choose a reference frame where  $\hat{H}_{\text{KS}}[\boldsymbol{\rho}](\mathbf{r})$  is always diagonal. In this case we can simplify the formalism decoupling spin up and spin down to obtain two separate set of equations – the spin-polarized TDKS equations.

In order to describe photoemission processes from first principles we have to describe the interface between the material and the vacuum. To this end we model a surface as a semi-periodic structure repeating itself along two directions identified by the lattice vectors  $\mathbf{a}_1$  and  $\mathbf{a}_2$  like in Fig. 2. In the figure we indicate with  $\mathbf{z}$  the non-periodic dimension.

Owing to the periodicity of the system we can describe the infinite surface with wavefunctions confined to the volume  $\Omega = \mathbf{a}_1 \times \mathbf{a}_2 \times \mathbb{R}$  where  $\mathbf{a}_1$  and  $\mathbf{a}_2$  span the planar primitive cell. On the surface, we express the wavefunctions as Bloch spinors  $\bar{\varphi}_{j\mathbf{k}}(\mathbf{r}) = e^{i\mathbf{k} \cdot \mathbf{r}} \bar{u}_{j\mathbf{k}}(\mathbf{r})$  where  $\bar{u}_{j\mathbf{k}}(\mathbf{r})$

is a spinor with the periodicity of the lattice and  $\mathbf{k}$  covers the first Brillouin zone (BZ) of the reciprocal space, which is bidimensional. Using Bloch spinors corresponds to exchanging

$$\left(\nabla - \frac{\mathbf{A}(t)}{c}\right)^2 \rightarrow \left(\nabla + i\mathbf{k} - \frac{\mathbf{A}(t)}{c}\right)^2 \quad (7)$$

in the KS Hamiltonian,  $\hat{H}_{\text{KS}}[\rho](\mathbf{r})$ , defined in (3). The KS equations describing the infinite surface is then cast into a set of equations for each value of  $\mathbf{k}$  coupled through  $\rho(\mathbf{r})$  which can be obtained from (1) integrating the Bloch spinors over the first BZ in Eq. (5) and (6).

### C. The t-SURFFP method

To derive a suitable formalism for photoemission with TDDFT in semi-periodic systems we employ the t-SURFF method<sup>24,25</sup>. This method was recently extended to TDDFT in finite systems<sup>30</sup> and we hereby present a further extension to the semi-periodic case that we name t-SURFFP.

To this end we partition the volume  $\Omega$  along the non-periodic dimension in two regions,  $A$  and  $B$ , as illustrated in Fig. 2. We assume that in region  $A$  electrons are fully interacting and described by the KS Hamiltonian  $\hat{H}_{\text{KS}}(t)$  while in  $B$  they are non-interacting and free. In other words we ask that the time-dependent Hamiltonian governing the evolution of the system,  $\hat{H}(t)$ , asymptotically reduces to an exactly solvable one,  $\hat{H}_{\text{V}}(t)$ , for all times

$$\hat{H}(t) = \begin{cases} \hat{H}_{\text{KS}}(t) & \text{for } \mathbf{r} \in A \\ \hat{H}_{\text{V}}(t) & \text{for } \mathbf{r} \in B \end{cases}. \quad (8)$$

In our scheme  $\hat{H}_{\text{V}}(t)$  is the Volkov Hamiltonian governing the dynamics of  $N$  non-interacting free electrons in  $\Omega$  driven by a time-dependent external field  $\mathbf{A}(t)$ ; in the velocity gauge this is expressed by

$$\hat{H}_{\text{V}}(t) = \sum_{j=1}^N \frac{1}{2} \left[ -i\nabla_j - \frac{\mathbf{A}(t)}{c} \right]^2 \sigma_0, \quad (9)$$

and is diagonal in spin-space as indicated by the presence of  $\sigma_0$ . Provided the vector field  $\mathbf{A}(t)$  is constant in space we can solve exactly the time dependent Schrödinger equation associated with  $\hat{H}_{\text{V}}(t)$ . For each single electron the solution can be written in the form of a plane wave spinor with momentum  $\mathbf{p}$

$$\bar{\chi}_{\mathbf{p}}(\mathbf{r}, t) = \sqrt{\frac{2\pi}{a_1 a_2}} e^{i\mathbf{p}\cdot\mathbf{r}} e^{-i\phi(\mathbf{p}, t)} \quad (10)$$

multiplied by a time-dependent phase factor

$$\phi(\mathbf{p}, t) = \frac{1}{2} \int_0^t d\tau \left[ \mathbf{p} - \frac{\mathbf{A}(\tau)}{c} \right]^2. \quad (11)$$

Each spinor is normalized on  $\Omega$  which is finite along  $\mathbf{a}_1$  and  $\mathbf{a}_2$  but infinite along  $\mathbf{z}$ , and the normalization factor precisely accounts for this geometry. Further, owing to periodic boundary conditions along  $\mathbf{a}_1$  and  $\mathbf{a}_2$ , we can decompose  $\mathbf{p}$  into a sum of a k-point  $\mathbf{k}$ , bound to the plane of the surface, and a general reciprocal lattice vector  $\mathbf{G}$ :  $\mathbf{p} = \mathbf{k} + \mathbf{G}$ . Owing to the periodicity of the system  $\mathbf{G}_{\parallel}$  assumes discrete values while  $\mathbf{G}_{\perp}$  is continuous. Since the wavefunctions in (10) are not pure Volkov waves but retain information about the periodic dimensions we denote them as Bloch-Volkov waves.

When the system ionizes we can make a further assumption on the spatial distribution of the wavefunction. In the long time limit, after the external field has been switched off ( $\mathbf{A}(t > T) = 0$ ), we assume that each KS spinor is factorizable into a bound and a scattering component localized in  $A$  and  $B$  respectively,

$$\bar{\varphi}_{j\mathbf{k}}(\mathbf{r}, t) = \bar{\varphi}_{j\mathbf{k},A}(\mathbf{r}, t) + \bar{\varphi}_{j\mathbf{k},B}(\mathbf{r}, t). \quad (12)$$

Under this assumption the number of electrons escaped per unit cell from  $A$  at time  $T$  can be expressed as

$$\begin{aligned} N_{\text{esc}}(T) &= \int_{\Omega} d\mathbf{r} n_B(\mathbf{r}, T) \\ &= \int_{\Omega} d\mathbf{r} \int_{BZ} d\mathbf{k} \sum_{j=1} \theta_j |\bar{\varphi}_{j\mathbf{k},B}(\mathbf{r}, T)|^2 \end{aligned} \quad (13)$$

where  $\theta_j$  is a shorthand for  $\theta(\mu - \epsilon_j)$  as in (5), and  $n_B(\mathbf{r}, T)$  is the charge density in  $B$ .

Since the Coulomb-Volkov waves form a complete set we can expand each KS spinor as

$$\bar{\varphi}_{j\mathbf{k},B}(\mathbf{r}, t) = \int d\mathbf{p} \bar{b}_j(\mathbf{p}) \chi_{\mathbf{p}}(\mathbf{r}, t), \quad (14)$$

where we defined the coefficients

$$\bar{b}_j(\mathbf{p}) \equiv \begin{bmatrix} b_{j+1/2}(\mathbf{p}) \\ b_{j-1/2}(\mathbf{p}) \end{bmatrix} \quad (15)$$

as column vectors in spin space. Inserting (14) into (13) we obtain that the number of escaped electrons can be expressed in terms of the expansion coefficients  $b_{j\alpha}(\mathbf{p})$  by tracing over the spin components as follows

$$N_{\text{esc}}(T) = \sum_{j=1} \theta_j \sum_{\alpha=-BZ}^+ \int d\mathbf{k} \int d\mathbf{p} |b_{j\alpha}(\mathbf{p})|^2. \quad (16)$$

The spinless momentum-resolved photoelectron probability  $\mathcal{P}(\mathbf{p})$  is thus naturally obtained from the former expansion as the derivative with respect to  $\mathbf{p}$  of  $N_{\text{esc}}(T)$

$$\mathcal{P}(\mathbf{p}) = \frac{\partial N_{\text{esc}}(T)}{\partial \mathbf{p}} = \sum_{j=1} \theta_j \sum_{\alpha=-BZ}^+ \int d\mathbf{k} |b_{j\alpha}(\mathbf{p})|^2. \quad (17)$$

In order to calculate  $\mathcal{P}(\mathbf{p})$  we thus need an explicit form for the expansion coefficients compatible with a TDDFT

formulation. This is provided by the flux of the photoelectron current through a closed surface.

Using the continuity equation we can express the number of escaped electrons as the flux of the current density  $\mathbf{J}(\mathbf{r}, t)$  through a surface  $S$  enclosing the system. By choosing  $S$  as in Fig. 2 parallel to the system's plane we have that

$$N_{\text{esc}}(T) = - \int_0^T d\tau \oint_S d\mathbf{s} \cdot \mathbf{J}(\mathbf{r}, \tau). \quad (18)$$

We are thus left with the task of connecting  $\mathbf{J}(\mathbf{r}, t)$  with the KS spinors. This is achieved observing that  $\mathbf{J}(\mathbf{r}, t)$  can be expressed as the expectation value of the single particle current density operator

$$\hat{\mathbf{j}}(t) = \frac{1}{2} \left[ \left( -i\nabla - \frac{\mathbf{A}(t)}{c} \right) + \text{c.c.} \right] \sigma_0 \quad (19)$$

over KS orbitals as follows

$$\mathbf{J}(\mathbf{r}, t) = \sum_{j=1} \theta_j \int_{BZ} d\mathbf{k} \langle \bar{\varphi}_{j\mathbf{k}}(t) | \hat{\mathbf{j}}(t) | \bar{\varphi}_{j\mathbf{k}}(t) \rangle. \quad (20)$$

We can then use (14) to expand the bra in the former equation to obtain

$$\mathbf{J}(\mathbf{r}, t) = \sum_{j=1} \theta_j \int_{BZ} d\mathbf{k} \int d\mathbf{p} \bar{b}_j^*(\mathbf{p}) \langle \chi_{\mathbf{p}}(t) | \hat{\mathbf{j}}(t) | \bar{\varphi}_{j\mathbf{k}}(t) \rangle \quad (21)$$

and the complex conjugated counterpart by expanding the ket

$$\mathbf{J}(\mathbf{r}, t) = \sum_{j=1} \theta_j \int_{BZ} d\mathbf{k} \int d\mathbf{p} \bar{b}_j(\mathbf{p}) \langle \bar{\varphi}_{j\mathbf{k}}(t) | \hat{\mathbf{j}}(t) | \chi_{\mathbf{p}}(t) \rangle. \quad (22)$$

Finally, by inserting (21) and (22) into (18) and directly comparing the resulting equations with (16) we arrive at an explicit equation for the Bloch-Volkov expansion coefficients in the form of flux integral

$$\bar{b}_j(\mathbf{p}) = - \int_0^T d\tau \oint_S d\mathbf{s} \cdot \langle \chi_{\mathbf{p}}(\tau) | \hat{\mathbf{j}}(\tau) | \bar{\varphi}_{j\mathbf{k}}(\tau) \rangle. \quad (23)$$

Further, by exposing the k-point dependence of each Bloch-Volkov spinor, we can recast the previous equation into a form containing only the periodic component of each KS orbital as

$$\bar{b}_j(\mathbf{p}) = - \int_0^T d\tau \oint_S d\mathbf{s} \cdot \langle \mathbf{G} | \hat{\mathbf{j}}(\tau) | \bar{u}_{j\mathbf{k}}(\tau) \rangle e^{i\phi(\mathbf{p}, \tau)}, \quad (24)$$

where  $|\mathbf{G}\rangle$  are planewaves of momentum  $\mathbf{G}$  normalized in  $\Omega$  as in Eq. (10). This formulation is particularly convenient for numerical implementations since it involves only the periodic spinors  $\bar{u}_{j\mathbf{k}}(\tau)$  and thus it fully exploits

the Bloch factorization of the KS equations discussed in Sec. IB.

Equation (24) together with (17) provide a straightforward way to calculate the spinless momentum-resolved photoelectron probability  $\mathcal{P}(\mathbf{p})$ . We recall that this result has been derived under the assumption that, (i) the Hamiltonian of the system can be well approximated with (8), and (ii) that scattering and bound electrons are spatially well separated at all times (12). In addition, by choosing TDDFT as working framework, we assumed that the longitudinal part of the photoelectron current is the one that contribute the most in the photoelectron spectrum. These conditions ultimately define the range of applicability of the method. They are clearly satisfied at an infinite distance from the system and close to the detectors where electrons can be safely considered free forward-moving particles, and poor in the vicinity of the surface. Positioning the sampling surface  $S$  is the only parameter controlling the accuracy of this approximation and, in practical calculations, it has to be varied until a convergence of the spectrum is achieved.

Once the expansion coefficients are calculated we can obtain the spin-density photoelectron probability  $\mathcal{P}_{\alpha\beta}(\mathbf{p}) = \mathbf{P}(\mathbf{p})$  with a procedure similar to the one employed to construct the spin-density matrix of Eq. (1), i.e. by simply substituting the spinors in the definitions of (5) and (6) with  $\bar{b}_j(\mathbf{p})$  and then use equation Eq. (1). The spin-resolved photoelectron probability polarized along the direction  $\mathbf{s}$  is obtained tracing over the spin dimension as follows

$$\mathcal{P}_{\mathbf{s}}(\mathbf{p}) = \text{Tr}[\mathbf{P}(\mathbf{p})\boldsymbol{\sigma} \cdot \mathbf{s}]. \quad (25)$$

The spinless photoelectron probability can also be obtained tracing out the spin degrees of freedom consistently with (17):  $\mathcal{P}(\mathbf{p}) = \text{Tr}[\mathbf{P}(\mathbf{p})]$ . The photoelectron spin polarization is then defined as the ratio between spin-resolved and spinless probabilities

$$\Pi_{\mathbf{s}}(\mathbf{p}) = \frac{\mathcal{P}_{\mathbf{s}}(\mathbf{p})}{\mathcal{P}(\mathbf{p})}. \quad (26)$$

From the knowledge of  $\mathcal{P}(\mathbf{p})$ , ARPES is directly obtained by looking at the electron photoemission probability as a function of the total kinetic energy  $E$  and the parallel component of the escaping momentum  $\mathbf{p}_{\parallel}$  as discussed in Sec. IA:  $\mathcal{P}(\mathbf{k}_{\parallel} = \mathbf{p}_{\parallel}, E = \frac{\mathbf{p}_{\parallel}^2}{2})$ .

Note that the external field  $\mathbf{A}(t)$  we use to derive the t-SURFFP equation (24) and to propagate the KS equations (3) is free to assume any arbitrary temporal shape. This means that it can describe any linear combination of laser fields. Our approach thus provides a straightforward environment to simulate tARPES where the time variable is extracted through the variation of a time-delay between two laser pulses in a pump-probe configuration.

## II. APPLICATIONS

### A. Computational details

We implemented the t-SURFFP method in the Octopus code<sup>43–45</sup>. In Octopus the TDKS equations are solved in a real-space grid and propagated in real-time. The real-space approach offers a great versatility when it comes to the description of semi-periodic systems as it naturally allows to impose mixed boundary conditions. The real-time propagation offers additional flexibility as it consents to describe external fields with arbitrary temporal shape. In our implementation we used the exact cutoff method described in Ref.<sup>46</sup> along the non-periodic dimension and employed non-orthogonal grids<sup>47</sup>, optimized according to the lattice symmetries, on the periodic ones. Our implementation is fully parallel in grid points, k-points, bands and spin dimension. For the largest systems presented in this paper (bilayer WSe<sub>2</sub>), we found that the distribution over only k-points and states is enough to saturate a medium-size cluster ( $\approx 1024$  cores).

In the code we use a pseudopotential formalism where only valence electrons are treated explicitly. Core electrons together with the ionic potential are replaced by an effective pseudopotential such that the ionic potential is composed of a local potential, a non-local one plus a SOC term

$$V_{\text{ion}}(\mathbf{r}) = V_{\text{local}}(\mathbf{r}) + V_{\text{nlocal}}(\mathbf{r}) + V_{\text{SO}}\mathbf{L} \cdot \mathbf{S}. \quad (27)$$

In all the calculations we used HGH pseudopotentials<sup>48</sup> accounting for relativistic effects only for the compounds containing W.

Further, we used the local density approximation (LDA)<sup>49</sup> to the exchange and correlation functional. For non-collinear spin configurations we treat the functional at the level of local spin-density approximation (LSDA) by rotating to the local reference frame where the spin density matrix is diagonal<sup>50</sup>.

In order to prevent spurious reflection on the non-periodic edges of the cell we employed complex absorbing-potential boundary conditions<sup>51</sup>. We tune the absorber parameters (width and imaginary amplitude) such that the boundary is effective in the energy window of the ejected photoelectrons<sup>52</sup>. Owing to the presence of absorbing boundaries the total charge in the cell is not conserved over time. To avoid artifacts from charge imbalance we chose the laser intensity such that the total charge loss is negligible. In our calculations we found that a  $10^{-4}\%$  of charge loss is sufficient to provide stable results.

In the following we present applications for three different materials having an hexagonal lattice. These are all stable layered structures that are currently in the focus of extensive research and for which a considerable amount of high quality experimental data is being produced. We stress however that the computational tool we

developed is by no means restricted to hexagonal crystal lattices only.

In all the simulations we used laser pulses that are zero everywhere except for  $t \in [0, T]$  with

$$\mathbf{A}(t) = \epsilon A_0 \sin\left(\frac{\pi t}{T}\right)^2 \cos(\omega t); \quad (28)$$

here  $\epsilon$  is the polarization axis,  $A_0$  is the peak amplitude and  $\omega$  the carrier frequency. This choice is motivated by the resemblance to the typical experimental Gaussian shape while retaining the property of being exactly zero outside a given time window – this is important to minimize the propagation time in the simulations. All the simulations have been carried out on a box of 120 au along the non-periodic dimension and centered around each system. Along the periodic dimension the box is taken according to the primitive cell of the system. Complex absorbing potentials of 30 au width have been placed at the opposite sides of the simulation box to prevent reflections. The t-SURFFP analyzing surface was placed at 30 a.u. from the edges right before the onset of the absorbers. Finally the first BZ was sampled by a  $12 \times 12$  grid of  $\mathbf{k}$ -points in reciprocal space for all the systems.

### B. Graphene

In this section we illustrate the application of t-SURFFP to simulate ARPES from graphene monolayer. To this end we ionize the system with a 50 fs laser pulse with  $\omega = 95$  eV,  $\epsilon = \mathbf{z}$ , and peak intensity  $I = 10^9$  W/cm<sup>2</sup>. In an experiment this geometry corresponds to the case where the laser is grazing with respect to the surface. In our calculations we used a grid spacing of 0.36 a.u. and a lattice constant of  $a = 4.65$  a.u..

The results of the simulation are illustrated in Fig. 3 (a) on the  $\Gamma$ -K-M- $\Gamma$  path in the BZ (see inset). ARPES presents intensity peaks that are positioned in excellent agreement with the DFT band structure (overlaid with red lines) and thus is in agreement with the interpretation of the ionization process in terms of the photoelectric effect.

Not all the DFT bands are visible in the spectrum. This behavior can be explained in first order time-dependent perturbation theory with Fermi's golden rule which describes the probability to excite an initial state in the material  $|i\rangle$  to final state in the continuum  $|f\rangle$  in terms of the dipole matrix element  $|\langle f|\hat{\mathbf{p}} \cdot \epsilon|i\rangle|^2$ . Final states that are connected with negligible matrix elements appear dark in the spectrum. The matrix element intensity effects observed in the calculation are in excellent agreement with the literature<sup>53</sup>.

Around the Dirac point, on the valence band close to K, graphene ARPES presents a peculiar intensity pattern. Only one branch of the Dirac cone is visible crossing K from a path along the  $\Gamma$ -K direction while both are visible from a direction parallel to  $\Gamma$ -M as shown in

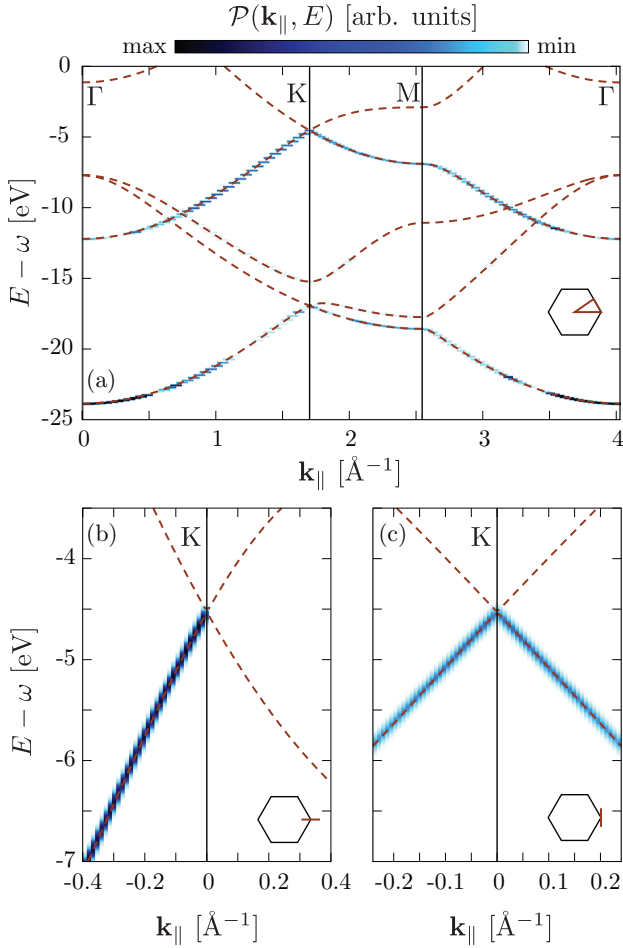


FIG. 3. Graphene ARPES as obtained using a 50 fs pulse with  $\omega = 95$  eV,  $\epsilon = \mathbf{z}$ , and peak intensity  $I = 10^9$  W/cm<sup>2</sup>. (a) ARPES cut along the  $\Gamma$ -K-M- $\Gamma$  path in the BZ, (b) cut along a direction parallel to  $\Gamma$ -K centered in K and (c) cut along a direction parallel to  $\Gamma$ -M also centered in K. In all panel the inset schematically represents the reciprocal space path on which the spectra are plotted, and the DFT band structure is overlaid in red.

Fig. 3 (b) and (c). This is a characteristic feature of ARPES on graphene which has been observed in many experiments<sup>53</sup> and that is due to the chiral character of Dirac states at the K point.<sup>54</sup>

In this work we do not include any dissipation channel. The finite line-width observed in ARPES is thus a direct consequence of the finite time window of the probe pulse. In principle, however, it could be possible to include dissipation, for instance, by coupling the electronics degrees of freedom with lattice vibrations using Ehrenfest theorem.<sup>55</sup>

### C. WSe<sub>2</sub>

In this section we turn to a system with a non-trivial spin configuration and study photoemission from the

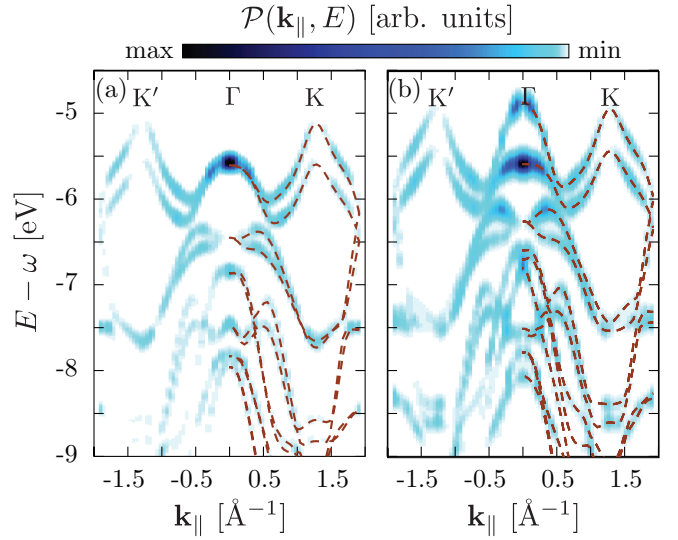


FIG. 4. ARPES on WSe<sub>2</sub> monolayer (a) and bilayer (b). To produce the spectra we used a 48 fs laser pulse with frequency  $\omega = 127$  eV, polarization  $\epsilon = \mathbf{z}$ , and peak intensity  $I = 10^9$  W/cm<sup>2</sup>. The ground state band structure is depicted in red.

transition metal dichalcogenide WSe<sub>2</sub>.

We probe the system with a 48 fs laser pulse polarized along  $\mathbf{z}$  with carrier frequency  $\omega = 127$  eV and peak intensity  $I = 10^9$  W/cm<sup>2</sup>. We performed the simulations with a grid spacing of 0.4 a.u., employed a lattice constant of  $a = 6.2$  a.u., and included semicore electrons in the pseudopotential for W. The results are presented in Fig. 4 (a) and (b) for monolayer and bilayer respectively.

As observed in the previous section the agreement between the ARPES spectrum and the equilibrium band structure is excellent. In addition, the results for the bilayer in Fig. 4 (b) is in good agreement with ARPES experiments recently reported on bulk WSe<sub>2</sub><sup>56,57</sup>. The reason for such agreement is related to the surface sensibility of ARPES experiments.<sup>9</sup> In fact, scattering prevents photoelectrons to be ejected from the lower lying layers of the material and effectively only the topmost layers at the surface contribute to the spectrum. By comparing this spectrum to the experiments reported in Refs.<sup>56,57</sup> it becomes clear that the system probed by the experiment is composed of more than two layers as indicated, for instance, by the presence of an ARPES signal filling the space between the two topmost valence bands at  $\Gamma$ .

In monolayer WSe<sub>2</sub> inversion symmetry is broken. For this reason the high-symmetry points K and K' in reciprocal space are no longer equivalent. This fact combined with a strong SOC provides a large splitting and polarization of the bands which is opposite for K and K'. Both splitting and spin polarization can be measured with sARPES as illustrated in Fig. 5 (a). According to sARPES the topmost valence bands at K and K' are fully spin polarized and with opposite spins. At  $\Gamma$ , where the

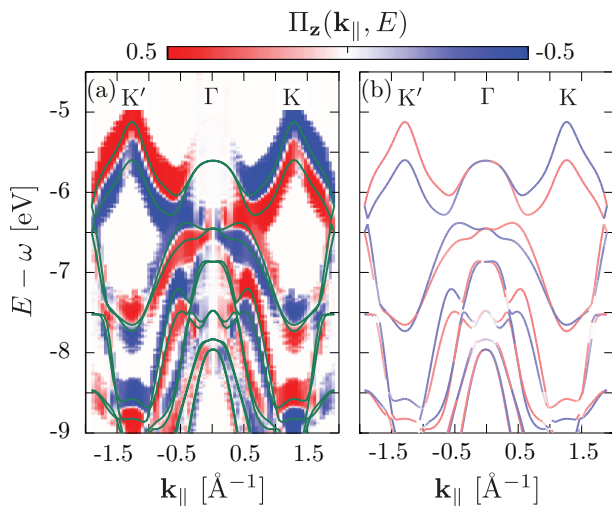


FIG. 5. Spin-resolved ARPES for monolayer WSe<sub>2</sub>. In panel (a) we show  $\Pi_z(\mathbf{k}_{\parallel}, E)$ , the photoelectron spin polarization spectrum along  $z$  overlaid with the band structure in green. In (b) is depicted the spin polarization of the ground state band structure. Laser parameters are the same as in Fig. 4.

bands are degenerate the spin polarization is zero. This behavior is consistent with the spin polarization of the DFT bands shown in Fig. 5 (a) where becomes apparent that the zero spin-polarization at  $\Gamma$  emerges from degenerate bands with opposite polarization.

#### D. Hexagonal Boron-nitride

In this section we explore the dimension offered by tARPES and illustrate the case of monolayer hBN in a pump and probe setup.

First we probe the system in its ground state with a 24 fs UV pulse linearly polarized 45° off-plane along one of the lattice vectors  $\epsilon_{\parallel} = \mathbf{a}_1$  with  $\omega = 40.8$  eV, and  $I = 10^{10}$  W/cm<sup>2</sup>. The simulations have been carried out with a grid spacing 0.36 a.u. and a lattice constant of  $a = 4.76$  a.u.. The resulting ARPES in Fig. 6 (a) is in good agreement with experimental data<sup>58</sup> and with the DFT band structure.

Next, we first pump the system with a laser pulse and probe it right after the pump is switched off. To this end we used a 20 fs in-plane pump pulse  $\epsilon = \mathbf{a}_1$  with  $\omega = 4.46$  eV,  $I = 2 \times 10^{11}$  W/cm<sup>2</sup> and then probe with a laser delayed of  $\Delta t = 20$  fs. The pump pulse is resonant with the gap at K and therefore it can excite electrons from the valence to the conduction band. This excitation is confirmed by the tARPES spectrum in Fig. 6 (b) where we observe a signal from electrons located on the conduction bands around both K and K'. This is a clear indication of a resonant population transfer from valence to conduction band and a simple demonstration of how the method presented here can be used to simulate the full dynamics of a pump-probe ARPES experiment.

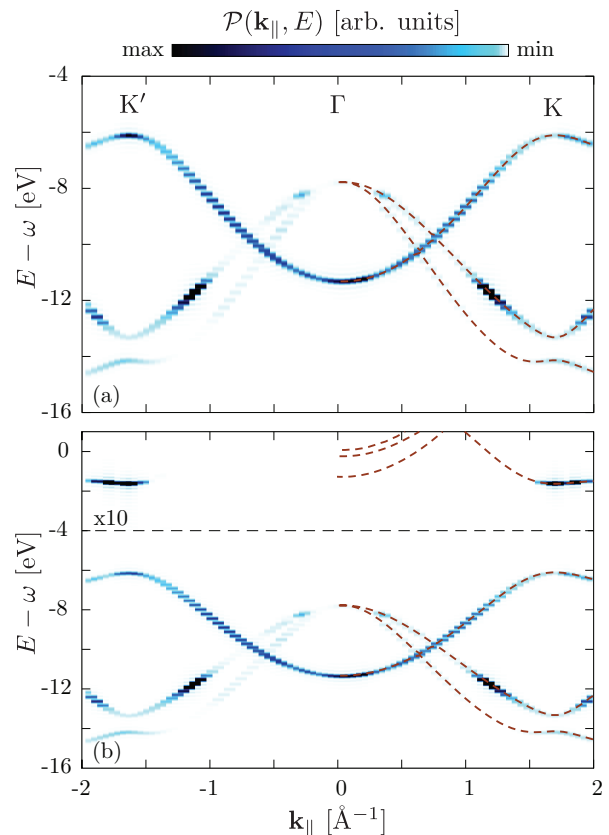


FIG. 6. Pump-probe ARPES on monolayer hBN. In (a) ARPES for the system in equilibrium probed by a 24 fs pulse polarized at 45° from the surface plane with  $\epsilon_{\parallel} = \mathbf{a}_1$ ,  $\omega = 40.8$  eV, and  $I = 10^{10}$  W/cm<sup>2</sup>. In (b) we show tARPES for the system pumped with a 20 fs pulse polarized in the plane of the surface  $\epsilon = \mathbf{a}_1$  resonant with the gap at K,  $\omega = 4.46$  eV,  $I = 2 \times 10^{11}$  W/cm<sup>2</sup> and probed by the same laser of panel (a) right after the pump is switched off,  $\Delta t = 20$  fs. ARPES signal on the conduction band is magnified by a factor 10. The band structure is overlaid in red on both panels.

### III. CONCLUSIONS

In this paper we have presented the t-SURFFP method – a novel ab-initio technique to simulate spin and time-resolved ARPES on semi-periodic systems based on TDDFT. This method makes no assumption on the probe pulse leaving polarization, energy and pulse shape (envelope) free to be chosen to closely match experimental conditions. The ionization dynamics is fully simulated by time-propagation of the electronic density under presence of the classical probe field fully accounting for electron-electron scattering, electron-ions scattering, surface image charge effects, classical screening and other dynamical effects, thus naturally including mean free path and matrix element effects. Quantum mechanical exchange and correlation effects, however, are approximated within the TDDFT framework through the exchange and correlation density functional. This lat-



ter approximation imposes some limitations to systematically describe strongly correlated systems and many-body effects, but for some cases specialized functionals exist. By accounting for the spin degree of freedom of the electrons this method also utilizes the extension of TDDFT to spin density dynamics to simulate spin-resolved ARPES measurements. The fully flexible definition of the external fields together with the first principles propagation of the density allows to create complex pump-probe setups where the electronic structure is excited separately by arbitrary pump pulses. This feature in particular allows for the first time the fully ab initio study of non-equilibrium electron dynamics under pump probe conditions with a large variety of applications.

We have thus introduced a versatile and general computational method for the ab-initio study and simulation

of photoemission experiments.

#### IV. ACKNOWLEDGMENTS

We acknowledge financial support from the European Research Council (ERC-2015-AdG-694097), Spanish grant (FIS2013-46159-C3-1-P), Grupos Consolidados (IT578-13), AFOSR Grant No. FA2386-15-1-0006 AOARD 144088, and European Unions Horizon 2020 Research and Innovation program under Grant Agreements no. 676580 (NOMAD) and 646259 (MOSTOPHOS). H.H. acknowledges support from the People Programme (Marie Curie Actions) of the European Union's Seventh Framework Programme FP7- PEOPLE-2013-IEF project No. 622934.

- 
- \* umberto.degiovannini@gmail.com  
 † hannes.huebener@gmail.com  
 ‡ angel.rubio@mpps.de
- <sup>1</sup> S. Hüfner, *Photoelectron Spectroscopy*, Advanced Texts in Physics (Springer Berlin Heidelberg, Berlin, Heidelberg, 2003).
  - <sup>2</sup> A. Damascelli, Z. Hussain, and Z.-X. Shen, *Rev. Mod. Phys.* **75**, 473 (2003).
  - <sup>3</sup> F. Krausz and M. I. Stockman, *Nat. Photon.* **8**, 205 (2014).
  - <sup>4</sup> J. Sánchez-Barriga, E. Golias, A. Varykhalov, J. Braun, L. V. Yashina, R. Schumann, J. Minár, H. Ebert, O. Kornilov, and O. Rader, *Phys. Rev. B* **93**, 155426 (2016).
  - <sup>5</sup> M. Lisowski, P. A. Loukakos, A. Melnikov, I. Radu, L. Ungureanu, M. Wolf, and U. Bovensiepen, *Phys. Rev. Lett.* **95**, 137402 (2005).
  - <sup>6</sup> A. L. Cavalieri, N. Müller, T. Uphues, V. S. Yakovlev, A. Baltuska, B. Horvath, B. Schmidt, L. Blümel, R. Holzwarth, S. Hendel, M. Drescher, U. Kleineberg, P. M. Echenique, R. Kienberger, F. Krausz, and U. Heinzmann, *Nature* **449**, 1029 (2007).
  - <sup>7</sup> T. Rohwer, S. Hellmann, M. Wiesenmayer, C. Sohrt, A. Stange, B. Slomski, A. Carr, Y. Liu, L. M. Avila, M. Källäne, S. Mathias, L. Kipp, K. Rossnagel, and M. Bauer, *Nature* **471**, 490 (2011).
  - <sup>8</sup> S. Neppl, R. Ernstorfer, A. L. Cavalieri, C. Lemell, G. Wachter, E. Magerl, E. M. Bothschafter, M. Jobst, M. Hofstetter, U. Kleineberg, J. V. Barth, D. Menzel, J. Burgdörfer, P. Feulner, F. Krausz, and R. Kienberger, *Nature* **517**, 342 (2015).
  - <sup>9</sup> R. Bertoni, C. W. Nicholson, L. Waldecker, H. Hübener, C. Monney, U. De Giovannini, M. Puppin, M. Hoesch, E. Springate, R. T. Chapman, C. Cacho, M. Wolf, A. Rubio, and R. Ernstorfer, (2016), 1606.03218.
  - <sup>10</sup> D. Hsieh, Y. Xia, D. Qian, L. Wray, J. H. Dil, F. Meier, J. Osterwalder, L. Patthey, J. G. Checkelsky, N. P. Ong, A. V. Fedorov, H. Lin, A. Bansil, D. Grauer, Y. S. Hor, R. J. Cava, and M. Z. Hasan, *Nature* **460**, 1101 (2009).
  - <sup>11</sup> D. Hsieh, Y. Xia, L. Wray, D. Qian, A. Pal, J. H. Dil, J. Osterwalder, F. Meier, G. Bihlmayer, C. L. Kane, Y. S. Hor, R. J. Cava, and M. Z. Hasan, *Science* **323**, 919 (2009).
  - <sup>12</sup> S.-Y. Xu, Y. Xia, L. A. Wray, S. Jia, F. Meier, J. H. Dil, J. Osterwalder, B. Slomski, A. Bansil, H. Lin, R. J. Cava, and M. Z. Hasan, *Science* **332**, 560 (2011).
  - <sup>13</sup> C. Jozwiak, C.-H. Park, K. Gotlieb, C. Hwang, D.-H. Lee, S. G. Louie, J. D. Denlinger, C. R. Rotundu, R. J. Birge-neau, Z. Hussain, and A. Lanzara, *Nature Phys.* **9**, 293 (2013).
  - <sup>14</sup> J. B. Pendry, *Surface Science* **57**, 679 (1976).
  - <sup>15</sup> C. N. Berglund and W. E. Spicer, *Phys. Rev.* **136**, A1030 (1964).
  - <sup>16</sup> G. D. Mahan and E. W. Plummer, in *Handbook of Surface Science*, edited by K. Horn and M. Scheffler (2000) pp. 1–35.
  - <sup>17</sup> J. Koringa, *Physica* **13**, 392 (1947).
  - <sup>18</sup> W. Kohn and N. Rostoker, *Phys. Rev.* **94**, 1111 (1954).
  - <sup>19</sup> H. Ebert, D. Ködderitzsch, and J. Minár, *Rep. Prog. Phys.* **74**, 096501 (2011).
  - <sup>20</sup> A. M. Uimonen, G. Stefanucci, and R. van Leeuwen, *J. Chem. Phys.* **140**, 18A526 (2014).
  - <sup>21</sup> B. Moritz, T. P. Devereaux, and J. K. Freericks, *Phys. Rev. B* **81**, 165112 (2010).
  - <sup>22</sup> M. Sentef, A. F. Kemper, B. Moritz, J. K. Freericks, Z.-X. Shen, and T. P. Devereaux, *Physical Review X* **3**, 041033 (2013).
  - <sup>23</sup> J. Braun, R. Rausch, M. Potthoff, J. Minár, and H. Ebert, *Phys. Rev. B* **91**, 035119 (2015).
  - <sup>24</sup> L. Tao and A. Scrinzi, *New J. Phys.* **14**, 013021 (2012).
  - <sup>25</sup> A. Scrinzi, *New J. Phys.* **14**, 085008 (2012).
  - <sup>26</sup> V. P. Majety, A. Zielinski, and A. Scrinzi, *J. Phys. B: At. Mol. Opt. Phys.* **48**, 025601 (2015).
  - <sup>27</sup> V. P. Majety, A. Zielinski, and A. Scrinzi, *New J. Phys.* **17**, 063002 (2015).
  - <sup>28</sup> A. Zielinski, V. P. Majety, S. Nagele, R. Pazourek, J. Burgdörfer, and A. Scrinzi, *Phys. Rev. Lett.* **115**, 243001 (2015).
  - <sup>29</sup> A. Zielinski, V. P. Majety, and A. Scrinzi, *Phys. Rev. A* **93**, 023406 (2016).
  - <sup>30</sup> P. Wopperer, U. De Giovannini, and A. Rubio, (2016), 1608.02818.
  - <sup>31</sup> A. Einstein, *Ann. Phys.* **31**, 132 (1905).
  - <sup>32</sup> A. N. Grigorenko, M. Polini, and K. S. Novoselov, *Nat. Photon.* **6**, 749 (2012).
  - <sup>33</sup> J. Lischner, D. Vigil-Fowler, and S. G. Louie, *Phys. Rev. Lett.* **110**, 146801 (2013).

- <sup>34</sup> F. Caruso and F. Giustino, Phys. Rev. B **92**, 045123 (2015).
- <sup>35</sup> U. Höfer, I. L. Shumay, C. Reuß, U. Thomann, W. Wal-lauer, and T. Fauster, Science **277**, 1480 (1997).
- <sup>36</sup> G. Mahan and E. W. Plummer, in *Handbook of Surface Science*, edited by K. Horn and M. Scheffler (2000) pp. 1–35.
- <sup>37</sup> U. von Barth and L. Hedin, J. Phys. Condens. Matter **5**, 1629 (1972).
- <sup>38</sup> G. F. Giuliani and G. Vignale, *Quantum theory of the elec-tron liquid* (Cambridge Univ. Press, Cambridge, 2005).
- <sup>39</sup> E. Runge and E. Gross, Phys. Rev. Lett. **52**, 997 (1984).
- <sup>40</sup> M. A. L. Marques, N. T. Maitra, F. Nogueira, E. Gross, and A. Rubio, *Fundamentals of Time-Dependent Density Functional Theory* (Springer-Verlag, 2011).
- <sup>41</sup> R. Baer, L. Kronik, and S. Kmmel, eds., *Open problems and new solutions in time dependent density functional theory*, Chemical Physics, Vol. 391 (Elsevier, 2011) pp. 1–176.
- <sup>42</sup> W. Kohn, Rev. Mod. Phys. **71**, 1253 (1999).
- <sup>43</sup> M. A. L. Marques, G. F. Bertsch, and A. Rubio, Comput. Phys. Commun. **151**, 60 (2003).
- <sup>44</sup> A. Castro, H. Appel, M. J. T. Oliveira, C. A. Rozzi, X. An-drade, F. Lorenzen, M. A. L. Marques, E. Gross, and A. Rubio, Phys. Status Solidi B **243**, 2465 (2006).
- <sup>45</sup> D. Strubbe, U. De Giovannini, A. H. Larsen, A. Varas, I. Theophilou, N. Helbig, M. J. Verstraete, L. Stella, A. Aspuru-Guzik, and A. Castro, PCCP (2015).
- <sup>46</sup> C. A. Rozzi, D. Varsano, A. Marini, E. Gross, and A. Ru-bio, Phys. Rev. B **73**, 205119 (2006).
- <sup>47</sup> A. Natan, A. Benjamini, D. Naveh, M. Tiago, S. Beckman, and J. R. Chelikowsky, Phys. Rev. B **78**, 075109 (2008).
- <sup>48</sup> C. Hartwigsen, S. Goedecker, and J. Hutter, Phys. Rev. B **58**, 3641 (1998).
- <sup>49</sup> J. P. Perdew, Phys. Rev. B **23**, 5048 (1981).
- <sup>50</sup> J. Kübler, K. H. Höck, J. Sticht, and A. R. Williams, J. Phys. F **18**, 469 (1988).
- <sup>51</sup> A. H. Larsen, U. De Giovannini, and A. Rubio, in *Density-Functional Methods for Excited States* (Springer Interna-tional Publishing, Cham, 2015) pp. 219–271.
- <sup>52</sup> U. De Giovannini, A. H. Larsen, and A. Rubio, EPJ B **88**, 1 (2015).
- <sup>53</sup> A. Bostwick, T. Ohta, T. Seyller, K. Horn, and E. Roten-berg, Nature Phys. **3**, 36 (2006).
- <sup>54</sup> M. Mucha-Kruczyński, O. Tsyplyatyev, A. Grishin, E. Mc-Cann, V. I. Fal’ko, A. Bostwick, and E. Rotenberg, Phys. Rev. B **77**, 195403 (2008).
- <sup>55</sup> X. Andrade, A. Castro, D. Zueco, J. L. Alonso, P. Echenique, F. Falceto, and A. Rubio, J. Chem. Theory Comput. **5**, 728 (2009).
- <sup>56</sup> J. M. Riley, F. Mazzola, M. Dendzik, M. Michiardi, T. Takayama, L. Bawden, C. Granerod, M. Leandersson, T. Balasubramanian, M. Hoesch, T. K. Kim, H. Takagi, W. Meevasana, P. Hofmann, M. S. Bahramy, J. W. Wells, and P. D. C. King, Nature Phys. **10**, 835 (2014).
- <sup>57</sup> J. M. Riley, W. Meevasana, L. Bawden, M. Asakawa, T. Takayama, T. Eknapakul, T. K. Kim, M. Hoesch, S. K. Mo, H. Takagi, T. Sasagawa, M. S. Bahramy, and P. D. C. King, Nat. Nanotechnol. **10**, 1043 (2015).
- <sup>58</sup> D. Usachov, A. Fedorov, O. Vilkov, V. K. Adamchuk, L. V. Yashina, L. Bondarenko, A. A. Saranin, A. Grüneis, and D. V. Vyalikh, Phys. Rev. B **86**, 155151 (2012).